remote sensing

MDPI

Article

Rock Glacier Inventory of the Southwestern Pamirs Supported by InSAR Kinematics

Qiqi Ma [1,*] and Takashi Oguchi [1,2]

[1] Department of Natural Environmental Studies, Graduate School of Frontier Sciences, The University of Tokyo, Kashiwanoha 5-1-5, Kashiwa 277-8563, Chiba, Japan; oguchi@csis.u-tokyo.ac.jp
[2] Center for Spatial Information Science, The University of Tokyo, Kashiwanoha 5-1-5, Kashiwa 277-8568, Chiba, Japan
* Correspondence: maqiqi@csis.u-tokyo.ac.jp

Abstract: Although rock glaciers (RGs) are prevalent in the southwestern Pamirs, systematic studies on them are scarce. This article introduces the first inventory of RGs in the southwestern Pamirs, situated at the western edge of the High Mountain Asia region. The inventory, established through a combination of Google Earth optical imagery and Interferometric Synthetic Aperture Radar (InSAR) techniques, encompasses details on the locations, geomorphological parameters, and kinematic attributes of RGs. A total of 275 RGs were cataloged in an area of 55.52 km^2 from 3620 to 5210 m in altitude. Our inventory shows that most RGs in this region are talus-connected (213 landforms), with the highest frequency facing northeast (23%). The distribution of RGs thins from west to east and is more abundant in higher altitudes. The Shakhdara range to the south hosts a denser and more active population of RGs than the Shughnon range to the north, highlighting the influence of topography and precipitation. Overall, RGs in the southwestern Pamirs exhibit high activity levels, with active RGs predominating (58%). A comparison between active and transitional RGs showed no significant differences in elevation, temperature, and slope. Glacier-connected and glacier forefield-connected RGs demonstrated higher line-of-sight (LOS) velocities than talus-connected and debris-mantled slope-connected RGs, underscoring the significant impact of precipitation and meltwater on their activity.

Keywords: rock glaciers; inventory; the Pamirs; InSAR

Citation: Ma, Q.; Oguchi, T. Rock Glacier Inventory of the Southwestern Pamirs Supported by InSAR Kinematics. *Remote Sens.* **2024**, *16*, 1185. https://doi.org/10.3390/rs16071185

Academic Editors: Ramón Pellitero and Luis Miguel Tanarro García

Received: 28 February 2024
Revised: 25 March 2024
Accepted: 26 March 2024
Published: 28 March 2024

1. Introduction

Rock glaciers (RGs), pivotal elements in alpine periglacial landscapes, are complex formations of ice and rock that engage in a slow, gravity-driven movement. Typically situated above the timberline in alpine regions, RGs are visually distinct, featuring a characteristic front, lateral margins, and a ridge-and-furrow topography [1–4].

The impacts of climate change on RGs may lead to permafrost thawing and ice melting. This process can destabilize slopes and alter runoff patterns and water quality, thereby increasing the risks of geological disasters such as landslides, debris flows, and floods [5–7]. RGs serve as vital proxies for permafrost occurrence in cold mountain areas. Their lower altitudinal limits often mark the lower boundary of discontinuous regional permafrost [5,8–12]. The state of these landforms, whether intact (active and transitional) or relict, is instrumental in permafrost distribution models, aiding the prediction of permafrost presence in areas lacking field data [10]. Additionally, RGs are recognized for their role as natural water reservoirs [13]. Their unique thermal dynamics, involving slow thawing and latent heat exchange, combined with the cooling effect of ventilated coarse blocks at their surface, enable them to act as long-term hydrological reserves in high-mountain systems [1,14–17]. The study of RGs is essential for understanding paleoclimatic changes, managing geohazards, and maintaining vital water resources in high-altitude regions.

Their unique characteristics and multifaceted roles in environmental and climatic systems underscore the importance of comprehensive research on these dynamic landforms.

The High Mountain Asia (HMA) region, encompassing the Tibetan Plateau and surrounding mountain ranges such as the Himalayas, Karakoram, Tien Shan, and Pamirs, stands as one of the world's foremost high-altitude regions with periglacial landforms. This area is also notably susceptible to climate change impacts [18,19]. In-depth RG inventories have been developed for several parts of the HMA region, including the Himalayas [8,12,15,20–22], the Karakoram [5], the Tien Shan [23–25], the Gangdise Mountains [26], the southeastern Tibetan Plateau [16,27,28] and the western Kunlun Mountains [29]. However, the southwestern part of the Pamir region, recognized as a significant solid water storage area, still lacks a systematic and detailed RG inventory. Consequently, the regional characteristics and environmental significance of RGs in this part of the Pamirs remain largely unexplored.

Kinematics plays an essential role in discerning the activity (active, transitional, and relict) of RGs. This dynamic is pivotal in estimating ice storage volumes and a key indicator in evaluating permafrost extent. Intact RGs, encompassing both active and transitional forms, are crucial for accurately mapping permafrost zones [5,8,12]. However, traditional methods for assessing RG activity, often based on visual interpretation, are subject to significant variability due to the reliance on the observer's experience and subjective judgment [30]. Recognizing the limitations of subjective assessments, the International Permafrost Association (IPA) advocates adopting more objective and precise methods, such as Interferometric Synthetic Aperture Radar (InSAR). This technology has been effectively applied in the HMA region to extract the velocity of RGs, demonstrating its feasibility and reliability in enhancing the precision of kinematic studies [23–25,28,29,31–34]. The shift toward InSAR in RG research marks a significant advancement in permafrost studies, ensuring more standardized assessments of RG dynamics, which are essential for understanding permafrost behavior and its environmental implications.

This study presents a comprehensive inventory of RGs in the southwestern Pamirs. This inventory was compiled by manually delineating the boundaries of RGs. Additionally, we employed InSAR-processed data from the Sentinel-1 satellite from 2018 to 2020 to estimate surface velocities and infer RG kinematics. This detailed inventory adheres to the guidelines set by the IPA, ensuring comparability with future inventories that follow these standards. Significantly, this inventory represents this region's first systematic survey, contributing to closing the gap in global RG inventories.

2. Study area

2.1. Geomorphological Setting

The study area is located at the southwestern extremity of the Pamirs, at the western end of the HMA, spanning between latitudes 36.7°N and 37.7°N and from longitudes 71.5°E to 73.1°E (Figure 1a). This region, part of the Gorno-Badakhshan Autonomous Region in Tajikistan, is defined by the Gunt River to the north and the Pyanj River to the west and the south, covering an area of about 12,000 km^2.

The region's landscape is primarily shaped by the Shughnon and Shakhdara mountain ranges, with the Shakhdara River flowing between them (Figure 1c). The western section of the Shakhdara range, featuring Peak Mayakovsky at 6096 m a.s.l., runs north to south and elevates upward from the north. In contrast, the eastern section extends east to west, marked by rugged, steep peaks, including Karl Marx Peak (6723 m) and Peak Engels (6510 m), and showcases a dramatic elevation drop of over 3000 m to the Pyanj River valley. This section is characterized by steep, glaciated ridges and significant relief, with descents of up to 1000 m to the valleys carved by rivers. In comparison, the northern part of the Shakhdara River basin features a more gradual terrain.

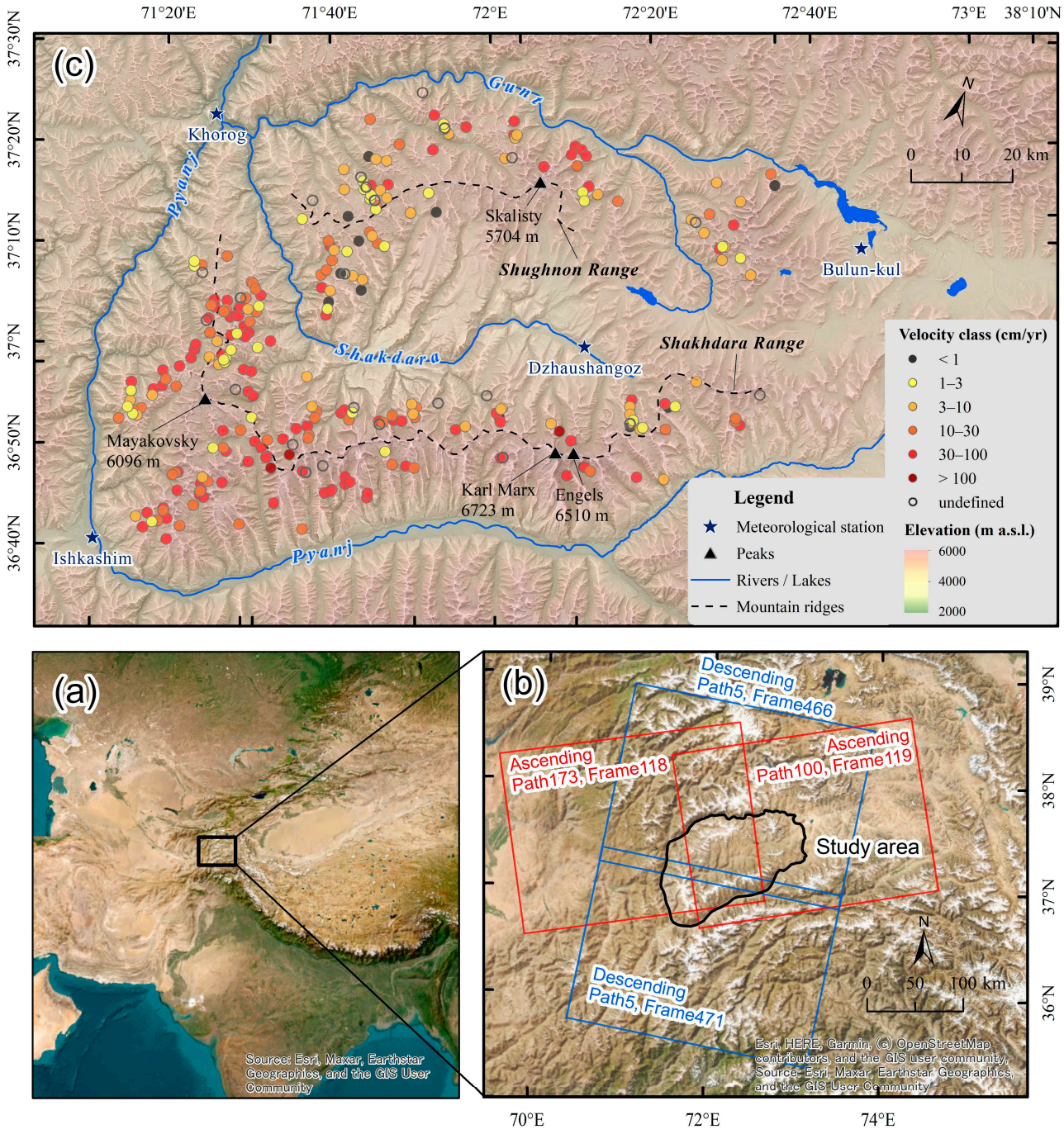

Figure 1. The study area and rock glaciers (RGs) in the southwestern Pamirs. (**a**) The location of the southwestern Pamirs. (**b**) The footprint of Sentinel-1 images. Red and blue boxes show the footprints of ascending and descending images, respectively. The black polygon outlines the study area. (**c**) The distribution of the mapped RGs in the southwestern Pamirs. Each RG is represented by a dot. The color of the dot represents the RG line-of-sight velocity class. Elevation colors and hill-shaded relief are created using the AW3D30 DEM.

Above 4500 m, the high-mountain regions are predominantly glacier-covered, with terrain playing a crucial role in their spatial distribution. The glaciers on the southern slopes are notably less extensive than those on the northern slopes. According to Mölg et al. [35], debris-covered glaciers are a frequent feature in this region.

2.2. Climate

The climate of the study area is semi-arid, predominantly influenced by the westerlies from the west. This climatic system brings significant cooling and precipitation during winter. The study area includes four meteorological stations: Kohrog (2075 m; 71.5316E, 37.4873N) and Ishakashim (2524 m; 71.600E, 36.7167N) in the Pyanj River valley, and Dzhaushangoz (3410 m; 72.4550E, 37.3569N) and Bulun-kul (3744 m; 72.9501E, 37.6998N) in the inner mountains. The mean annual air temperatures (*MAATs*) at Kohrog and Ishakashim are 9.3 °C and 7.3 °C, respectively, while Dzhaushangoz and Bulun-kul have recorded *MAAT* values of −1.6 °C and −5.6 °C between 1970 and 2008 [36]. The adiabatic rate is approximately −0.44 °C per 100 m in the valleys and −1.20 °C per 100 m in the mountainous areas, yielding an average adiabatic rate of about −0.93 °C per 100 m. Consequently, the zero-degree isoline is found at roughly 3200 m in altitude.

According to Maussion et al. [37], most precipitation (about 90%) occurs from December to May, with the northwestern areas receiving more rainfall. The climate becomes progressively drier and more continental, moving inland and eastward. The mean annual precipitation (MAP) at Kohrog and Ishakashim from 1970 to 2008 was 337 and 114 mm, respectively, in contrast to Dzhaushangoz and Bulun-kul, which recorded *MAP* values of 137 and 102 mm [36]. Precipitation levels in glacier and high-altitude areas (above 4000 m) are not well established, but data combining meteorological stations and models by Finaev et al. [36] suggest that the mountainous regions experience annual snow accumulations ranging from 400 to 700 mm w.e. (water equivalent).

3. Data and Methods

The manual delineation of RGs, leveraging InSAR and high-resolution optical imagery, adheres to the baseline concepts set forth by the IPA Action Group on Rock Glacier Inventories and Kinematics [38–40].

3.1. Rock Glacier Delineation

The outlines of RGs were delineated using high-resolution Google Earth imagery. These images, sourced from SPOT Images or Digital Globe products (e.g., Ikonos and QuickBird), offer a resolution comparable to aerial photographs (0.5–5 m) and are widely used in RG delineation [8,15,16,20,21]. We followed IPA guidelines as they provide practical and standardized baseline concepts for identifying and outlining RGs from remote sensing imagery, facilitating the generation of consistent inventories across extensive regions [38,39].

In the context of cold environments, such as uphill snow/ice patches, cirques, or glacial erosion features (e.g., over-deepening or receding backwalls), specific landforms that may exhibit rock glacier-like morphology (e.g., solifluction lobes and earth flows) were excluded. Other glacier- or paraglacial-related landforms (e.g., debris-covered glaciers, moraines, and pronival/protalus ramparts) were differentiated based on definitions described in the IPA guidelines and other studies (Table 1).

Based on their upslope connection units, RGs have been categorized into five distinct types: talus-connected RGs (T-RGs), debris-mantled slope-connected RGs (DMS-RGs), landslide-connected RGs (L-RGs), glacier-connected RGs (G-RGs), and glacier forefield-connected RGs (GF-RGs).

Due to the challenge of identifying the upper boundaries of T-RGs and DMS-RGs solely through ortho imagery, we utilized Google Earth, which provides 3D terrain features for digital mapping. The connection zones between talus deposits and RGs typically exhibit concave forms [39]. The upper boundaries of RGs were delineated where the slope at the base of the talus becomes gentler. Changes in texture, such as an increase in grain size and the presence of ice patches, were also employed as criteria to distinguish talus slopes from RGs. DMS-RGs lack prominent talus or headwalls upstream, and embedding the debris-mantled slope (source zone) into the RG footprint is advised against [38]. Consequently, their upper boundaries are conservatively estimated, relying on the characteristics of bulging due to ice content within RGs to determine the upper limits.

Table 1. Geomorphic indicators used for the differentiation of rock glaciers and other landforms.

Landforms	Geomorphic Indicators	References
Rock Glacier	Light-colored, steep frontal slope Swollen body Longitudinal or transversal ridges and furrows	[21,38]
Debris-covered glacier	Crevasses with exposed ice Thermokarst or supraglacial lakes Ice cliffs Supraglacial streams/channels	[21]
Moraine	Located in the margins of glaciers Broadly arcuate but often irregular and winding Single-crested ridge	[41]
Pronival/Protalus rampart	Single or double ridges No glacial erosional forms or evidence of over-deepening of the associated backwall area Lobate and insufficient cross-section for snow-to-glacier ice transformation	[42]

We employed the updated glacier inventory for Karakoram and Pamir [35] to identify surrounding glacier units. Subsequently, indicative features like the appearance of ice cliffs, supraglacial meltwater channels, or ponds, as detailed in [38], were used to differentiate debris-covered glaciers, G-RGs, and GF-RGs. We found no L-RGs in the southwestern Pamirs.

The RG metrics used in this study comprise length (m), area (km^2), minimum elevation at the front (*MEF*; m), maximum elevation (*MaxE*; m), elevation (mean elevation; m), slope (mean slope of gradient; °), and aspect (N, NE, E, SE, S, SW, W, and NW; e.g., 90° = E, 180° = S). They were calculated in ArcGIS 10.8 based on the AW3D30 DEM (https://www.eorc.jaxa.jp/ALOS/en/dataset/aw3d30/aw3d30_e.htm; accessed on 27 August 2022) with a spatial resolution of ~30 m. The RGs were categorized into tongue-shaped (i.e., length/width > 1) and lobe-shaped (i.e., length/width < 1) based on their shapes. The distribution of RGs was compared with the Permafrost Zonation Index (*PZI*) map [43] to analyze the relationship between RGs and permafrost. Modeled *MAAT* was extracted from air temperature grids with the *PZI* data for 1961–1990 [43].

3.2. InSAR Kinematics

Interferometric Synthetic Aperture Radar (InSAR) is an established technology for mapping surface displacements. It utilizes two SAR images acquired from slightly different orbital configurations and at different times to leverage the phase difference of the signals [44]. The interferometric phase comprises a topographic phase term, a displacement phase term, and error terms, including atmospheric distortion and system noise [44,45]. The core principle of differential SAR interferometry lies in isolating the topography- and displacement-related phase terms. This separation facilitates the mapping of coherent displacements occurring along the line of sight (LOS) between the acquisitions of the interferometric image pair. The systematic acquisitions and extensive spatial coverage offered by the latest generation of satellites, such as Sentinel-1, position InSAR as the most suitable tool for the objectives of this study [46].

Data from the Copernicus Sentinel-1 radar, specifically the Level-1 Single-Look Complex (SLC) products for the southwestern Pamirs, were downloaded from the Alaska Satellite Foundation Vertex website (https://vertex.daac.asf.alaska.edu; accessed on 8 August 2023). Our selection criteria focused on data captured in the interferometric-wide (IW) swath mode between 2018 and 2020. We specifically chose SAR images taken during July, August, and September, when the RGs in the southwestern Pamirs were predominantly snow-free. SAR scenes were downloaded for ascending track 100 frame 119 and track 173 frame 118 (with the satellite moving north and looking east), along with descending

track 5 frame 466 and track 5 frame 471, with the satellite moving south and looking west (Figure 1b). Each SAR scene features a pixel size of 14.1 m in azimuth (i.e., along-track direction) and 2.3 m in range (i.e., look direction).

Interferograms were processed using the Sentinel Application Platform (SNAP), a free and open-source toolbox provided by the European Space Agency (ESA). The processing was executed with two looks in range and one look in azimuth, yielding a pixel size of approximately 5 × 14 m. Following geocoding and Range Doppler terrain correction, the interferograms generated for kinematic analysis have an approximate resolution of 14 × 14 m. For each summer period (i.e., the snow-free interval), all serviceable combinations of interferograms were processed, as shown in Table A1. We selected images from different years to create year-long pairs that span the winter season when the ground is covered in snow. This approach resulted in the generation of 33 ascending and 33 descending pairs, culminating in 66 interferograms.

InSAR processing involves calculating the interferometric phase differences (i.e., the interferograms) from pairs of images with varying time intervals ranging from a few days to a year. Following geometric, topographic, and atmospheric corrections, the interferograms provide quantitative measurements of surface movements.

The subsequent step involves assigning a kinematic attribute to each identified RG, adhering to the guidelines of the RGIK [40]. The guideline states that "kinematic attributes are semi-quantitative (order of magnitude) information that should represent the overall multiyear downslope movement rate of the surveyed RGs". Thus, they reflect the kinematic behavior of the RGs.

Our analysis employed a manual approach using wrapped differential interferograms, computable over time intervals ranging from a few days to one year. Although manual analysis is time-intensive, it is a standard method in geomorphology and offers the advantage of interpreting decorrelated regions, which would be omitted in phase unwrapping. Furthermore, errors in phase unwrapping, inevitable with rough terrain with significant motion, are not easily identifiable by non-InSAR specialists and can lead to biased interpretations of fast-moving objects. Following the suggestions of the RGIK [40], we decided not to project the LOS velocity along the maximum slope direction because this would introduce further uncertainties, particularly when the LOS and slope direction approach a perpendicular direction.

The detectable range of movement depends on the interferogram's temporal interval, spatial resolution, and the satellite's wavelength [32,45,47,48]. The Sentinel-1 data operate in the C-band with a wavelength of 5.5 cm. A complete phase cycle corresponds to a change of half the wavelength in the LOS direction, approximately 2.75 cm. The time intervals for the image pairs in a year are 12, 24, 36, and 48 days, while for cross-year pairs, they range from 324 to 408 days. For example, a 12-day interferogram with a half-phase cycle (equivalent to 2.75/2 cm in 12 days, i.e., 42 cm/yr) is classified as 30–100 cm/yr. For a 36-day interferogram, a fringe pattern becomes undetectable (Figure 2b), and a half-phase cycle becomes visible with a 384-day interferogram (corresponding to 2.75/2 cm in 384 days, i.e., 1.3 cm/yr), classified as 1–3 cm/yr (Figure 2d). All velocity classes are shown in Figure 1c.

Following the RGIK's updated activity classification [40], RGs with velocities lower than 1 cm/yr were signed as "relict", RGs with velocities between 1 and 10 cm/year as "transitional", and RGs with higher velocities as "active". Notably, in this revised categorization, the traditional class of "inactive" is no longer utilized.

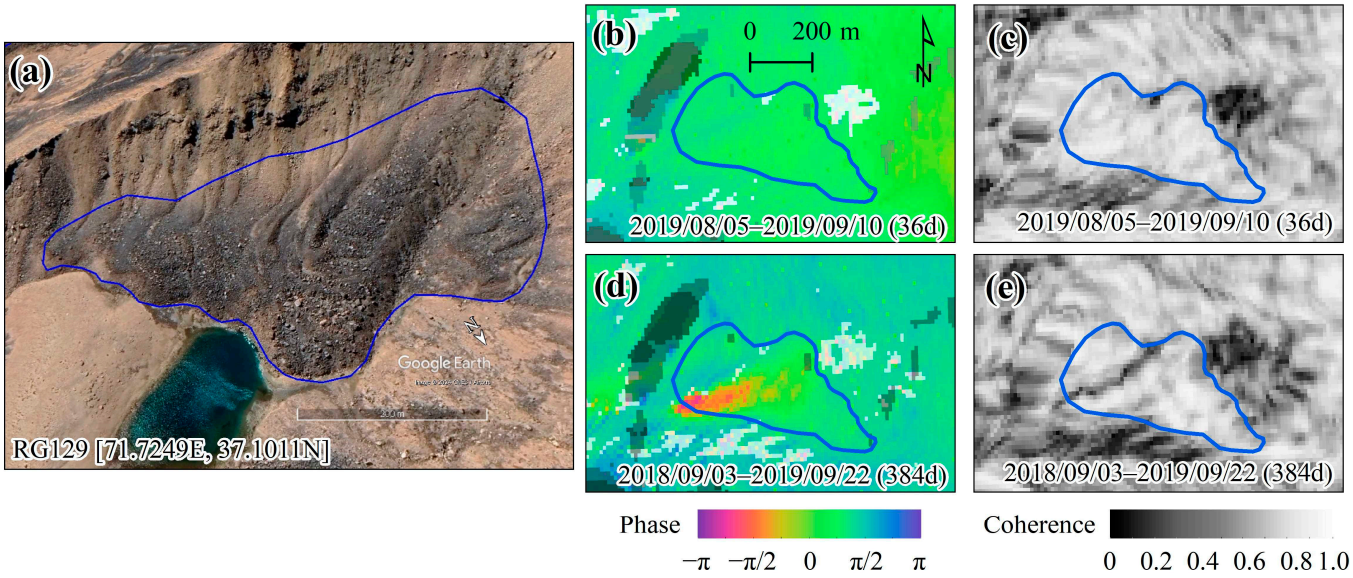

Figure 2. Examples of InSAR analysis for rock glacier kinematics. (**a**) Oblique view of RG129 on Google Earth. Blue line outlines the boundary of the rock glacier. (**b**,**d**) Interferograms over 36 and 384 days, respectively, where black pixels represent layover or shadow, and white pixels denote areas masked due to coherence less than 0.35. (**c**,**e**) Coherence for 36-day and 384-day interferograms, respectively.

3.3. Quality Control of the Interferograms

Despite the potential of InSAR, it also presents certain limitations. Firstly, the displacement measurements can be obscured by artifacts resulting from uncorrected atmospheric delays [29,34,46] and decorrelation or phase shifts due to changes in surface physical properties, such as vegetation, snow, and soil moisture [25]. To mitigate these limitations, it is crucial to exclude areas of decorrelation and rely on a stack of several interferograms from different periods. Therefore, we masked out pixels with coherence lower than 0.35. The RGIK [40] recommends using imagery spanning at least two years. In this study, Sentinel-1 data between 2018 and 2020 were utilized to ensure that each region had at least two interferograms from different years. This approach effectively removed the aforementioned interferences and minimized potentially large inter-annual variations in the movement rate of RGs.

Secondly, steep terrain in mountainous regions is often obscured by geometric distortions known as layover and shadow [47]. To reduce these constraints, this work employed both ascending and descending images from Sentinel-1. The selection of the best geometry is based on the direction of each RG [32,47,49,50].

Finally, due to the climatic characteristics of the study area, only snow-free summer images could be selected for velocity estimation, an unavoidable limitation in high-mountain regions [23,25,33]. This leads to uneven temporal intervals between image pairs, with intra-annual velocity estimates based on 12- to 48-day temporal baselines and inter-annual rates relying on ~408-day baselines. However, RG velocities vary seasonally, typically decreasing in winter [49,51–53]. The acceleration of RGs in spring and summer depends on meltwater and precipitation infiltrating into the RG shear zone, increasing pore pressure and reducing the overall material strength [54–58]. Consequently, the annual average velocities extrapolated from the summer observations may be overestimated. To address this, we selected as many image pairs as possible and examined the consistency of RG movement across different temporal spans. For instance, within the same year, the movement observed in 48-day interferograms should be greater than that in 36-day or 24-day interferograms, thereby mitigating the effects mentioned above.

4. Results

4.1. Geomorphic Characteristics of Rock Glaciers

In the southwestern Pamir region, our survey identified a total of 275 RGs, covering an area of 55.52 km^2 (Supplementary Materials). Morphologically, tongue-shaped RGs dominate the landscape, numbering 255, while lobate-shaped ones are relatively scarce, with only 20 instances. Regarding their spatial connection to the upslope unit, talus-connected RGs (T-RGs) are the most prevalent in terms of both area and quantity, accounting for over three-quarters of the total (213 RGs, covering 42.38 km^2). Although debris-mantled slope-connected RGs (DMS-RGs) outnumber glacier-connected RGs (G-RGs) and glacier forefield-connected RGs (GF-RGs), they contribute a smaller area (3.54 km^2) compared to the latter two categories (G-RGs: 4.06 km^2 and GF-RGs: 5.53 km^2) (Table 2).

Table 2. A statistical summary of the geomorphic parameters of the mapped rock glaciers (RGs) in the southwestern Pamirs.

Upslope Connection	Count	Total Area (km^2)	Area (km^2)	Length (m)	*MEF* (m a.s.l.)	*MaxE* (m a.s.l.)	Slope (°)	*MAAT* (°C)
T-RGs	213	42.38	0.20 (0.14)	894 (468)	4304 (248)	4562 (246)	16.7 (3.5)	−6.4 (1.4)
DMS-RGs	26	3.54	0.14 (0.07)	782 (377)	4234 (255)	4493 (225)	17.8 (3.8)	−5.8 (1.4)
G-RGs	14	4.06	0.29 (0.18)	989 (454)	4459 (261)	4673 (246)	14.5 (4.2)	−7.1 (1.4)
GF-RGs	22	5.54	0.25 (0.11)	871 (320)	4415 (237)	4640 (220)	15.0 (2.6)	−7.1 (1.3)
All RGs	275	55.52	0.20 (0.14)	887 (449)	4314 (252)	4568 (244)	16.5 (3.5)	−6.5 (1.4)

T-RGs: talus-connected RGs; DMS-RGs: debris-mantled slope-connected RGs; G-RGs: glacier-connected RGs; GF-RGs: glacier forefield-connected RGs; *MEF*: minimum elevation at the front; *MaxE*: maximum elevation; *MAAT*: mean annual air temperature. Each column presents the mean values of the geomorphic parameter followed by the corresponding standard deviations in the brackets.

We conducted a comparative analysis of geomorphological parameters across four categories of RGs. Due to non-normal distribution in several parameters like area, length, MEF, MaxE, and slope, we employed the non-parametric "Kruskal–Wallis ANOVA" test. MAAT, which conformed to a normal distribution, was analyzed using ANOVA.

Most RGs had areas between 0.05 and 0.35 km^2, with outliers larger than 0.5 km^2 predominantly being T-RGs. The area of DMS-RGs was significantly smaller than that of G-RGs and GF-RGs ($p < 0.01$). The average length of RGs was 887 m, with T-RGs and GF-RGs closely aligning with this value. G-RGs averaged about 100 m longer than the overall mean, while DMS-RGs were ~100 m shorter.

All RGs were situated within an elevation range from 3620 to 5210 m, with 80% located between 4100 and 4800 m (Figure 3a). The mean MEF and MaxE for RGs were 4314 ± 252 m and 4568 ± 244 m, respectively (Table 2). These mean values indicate that glacier-related landforms (G-RGs and GF-RGs) consistently occurred at higher elevations than talus-related landforms (T-RGs and DMS-RGs) (Table 2), with G-RGs having significantly higher MEF values than DMS-RGs ($p < 0.05$).

The elevation distribution for the other three groups was rather inhomogeneous. DMS-RGs were relatively evenly distributed between 4000 and 4600 m (Figure 3c), whereas G-RGs and GF-RGs were mostly found above 4400 and 4300 m (Figure 3d,e).

Most RGs had a mean slope of less than 20°, with T-RGs and DMS-RGs having slightly steeper average slopes (16.7° and 17.8°) compared to G-RGs and GF-RGs (14.5° and 15.0°) (Table 2). All RGs had an average *MAAT* value of −6.5 ± 1.4 °C. Both G-RGs and GF-RGs had an average *MAAT* value of −7.1 °C, significantly lower than that of DMS-RGs, which averaged at −5.8 °C ($p < 0.05$) (Table 2).

In the inventory, 49% (136) of the RGs were located on northeast-facing slopes (defined between N and E), with few on the south and southeast exposures (Figure 4a). The overall aspect distribution of RGs resembled that of T-RGs, with the most common orientations being northeast (23%) and southwest (15%) (Figure 4b). Nearly half (12 of 26) of the DMS-RGs faced north and northeast (Figure 4c), over half (12 of 22) of the GF-RGs faced east

and northeast (Figure 4d), and the majority of G-RGs were oriented toward the east (28%) (Figure 4e).

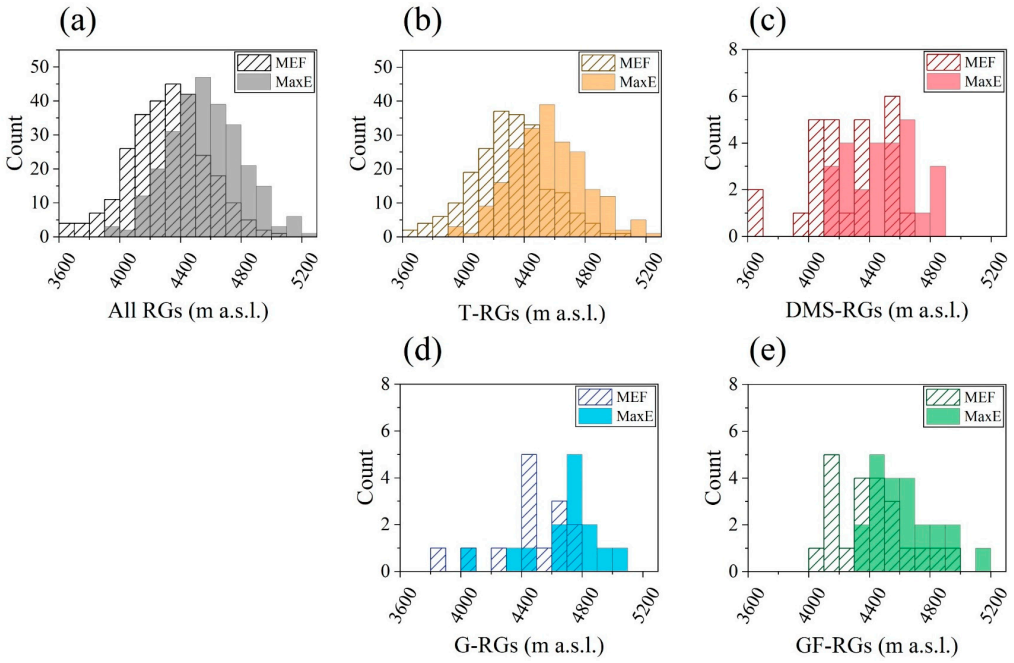

Figure 3. Histograms of the minimum elevation at the front (*MEF*) and maximum elevation (*MaxE*) for (**a**) all RGs, (**b**) talus-connected RGs (T-RGs), (**c**) debris-mantled slope-connected RGs (DMS-RGs), (**d**) glacier-connected RGs (G-RGs), and (**e**) glacier forefield-connected RGs (GF-RGs).

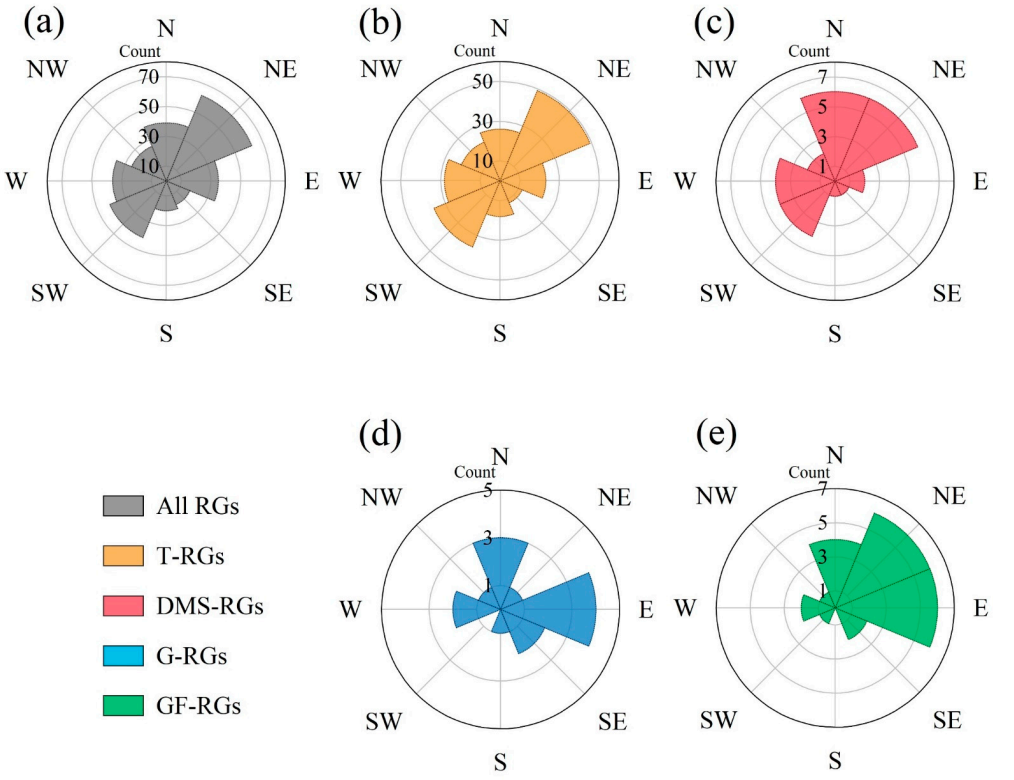

Figure 4. Histograms of the landform aspects for (**a**) all RGs, (**b**) talus-connected RGs (T-RGs), (**c**) debris-mantled slope-connected RGs (DMS-RGs), (**d**) glacier-connected RGs (G-RGs), and (**e**) glacier forefield-connected RGs (GF-RGs).

4.2. Distribution of Rock Glacier Kinematics

Valid kinematic attributes were obtained for 252 RGs, with 23 categorized as "undefined", yielding a detection rate of 91.6%. The overall distribution of LOS velocities for these RGs (Figure 5) indicates that the majority, over one-third, exhibit LOS velocities within the 30–100 cm/yr range. Nearly one-fourth fall within the 10–30 cm/yr range. Only six RGs exceed a LOS velocity of 100 cm/yr. Consequently, the predominant activity status in the southwestern Pamir RGs is "active", accounting for 159 landforms. RGs with LOS velocities of 1–3 cm/yr and 3–10 cm/yr constitute 14% and 19%, respectively, totaling 83 transitional RGs (TRGs). There are 10 relict RGs (RRGs).

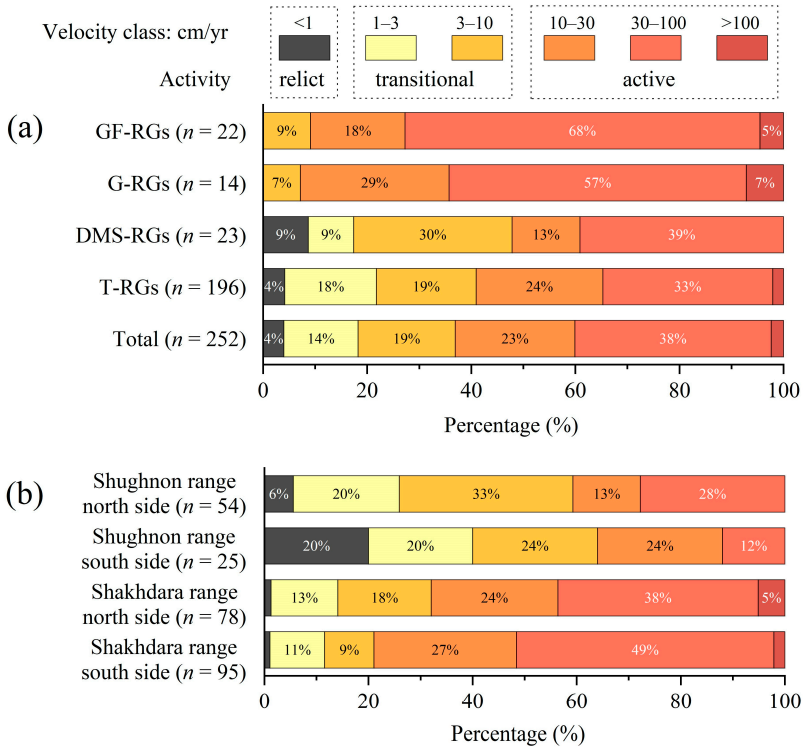

Figure 5. The distribution of the rock glacier (RG) kinematics for (**a**) the different connections of RGs (T-RGs: talus-connected RGs, DMS-RGs: debris-mantled slope-connected RGs, G-RGs: glacier-connected RGs, and GF-RGs: glacier forefield-connected RGs) and (**b**) the sides of mountain ranges. The length of the bars is proportional to the percentage (*X*-axis), and the values inside the bars indicate the proportion for each category.

Regarding different spatial connections to the upslope unit, the velocity distribution of T-RGs and DMS-RGs mirrors the overall trend, with active RGs (ARGs) outnumbering transitional ones and relict ones being the least common. Notably, in DMS-RGs, those with LOS velocities of 3–10 cm/yr (seven landforms) exceed those within the 10–30 cm/yr range (three landforms). In both G-RGs and GF-RGs, active RGs constitute over 90%, with more than half exhibiting LOS velocities of 30–100 cm/yr. No relict RGs are found in these two categories.

Spatially, the RGs in the Shakhdara range generally exhibit higher LOS velocities than those in the Shughnon range (Figure 5b). All six RGs faster than 100 cm/yr are located in the Shakhdara range. In this range, ARGs (128) are approximately three times more numerous than TRGs (43). On the southern slopes, ARGs account for 79%, while they constitute 68% on the northern slopes, with the most frequent contribution coming from those with LOS velocities between 30 and 100 cm/yr. ARGs on the south side of the Shakhdara range account for 79% of the total, while those on the north side constitute 68%. Among these ARGs, the number of rock glaciers with LOS velocities ranging from 30 to 100 cm/yr is the highest. In the Shughnon range, transitional RGs are slightly more

numerous than active ones, with 44% on the southern slopes and 53% on the northern slopes. Additionally, the southern slopes of the Shughnon range host the majority of the study area's RRGs (5 of 10).

4.3. Active Rock Glaciers and Transitional Rock Glaciers

A comparative analysis of the characteristics between ARGs and TRGs is shown in Figure 6. The frequency distribution of both area and length for ARGs and TRGs was similar (Figure 6a,b). However, ARGs were significantly larger in both area (0.23 ± 0.15 km^2) and length (1006 ± 478 m) compared to TRGs (0.17 ± 0.12 km^2; 770 ± 348 m) ($p < 0.01$). *MEF* and *MaxE* of both ARGs and TRGs exhibited a normal distribution (Figure 6c,d). TRGs had a slightly higher average *MEF* (4342 ± 227 m) than ARGs (4291 ± 259 m), while their average *MaxE* (4541 ± 222 m) was slightly lower than that of ARGs (4593 ± 248 m), suggesting that TRGs situate within a narrower elevation range of about 100 m compared to ARGs. Additionally, ARGs had a significantly steeper mean slope (17.8° ± 3.6°) compared to TRGs (14.9° ± 2.6°) ($p < 0.01$), with the majority of TRGs having a mean slope less than 20°. A total of 27.5% (44) of ARGs had slopes exceeding 20° (Figure 6e). There was no significant difference in *MAAT* between the two groups (Figure 6f).

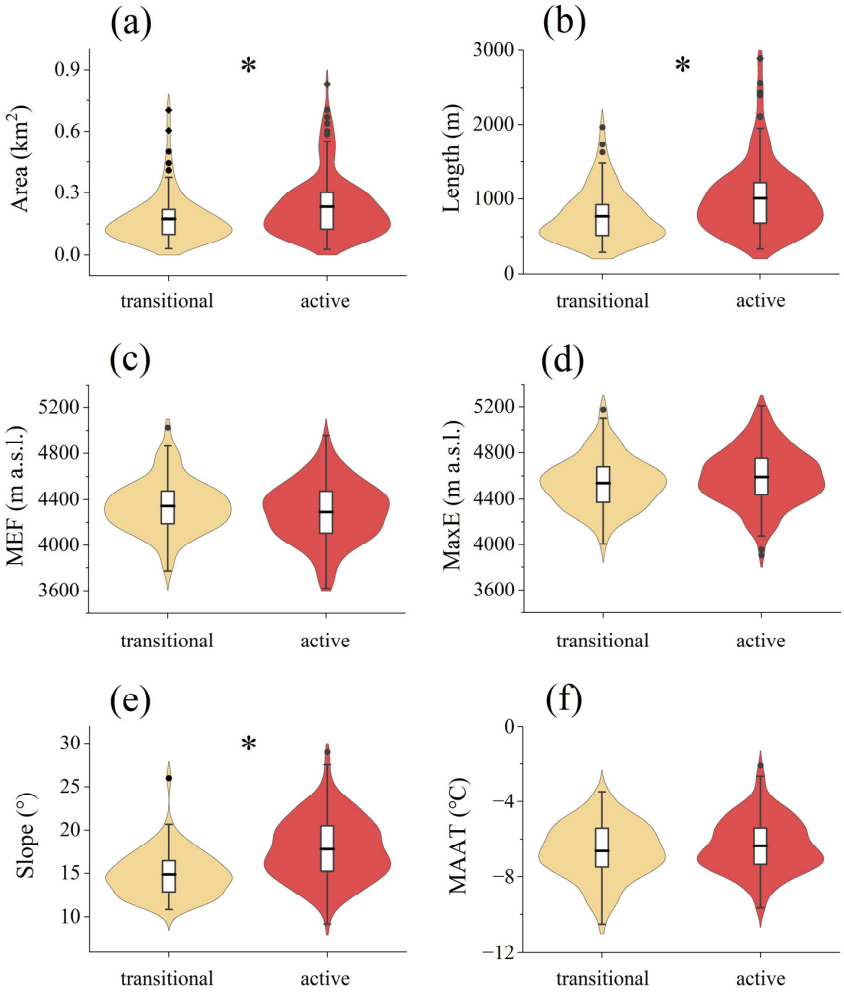

Figure 6. The characteristics of active RGs and transitional RGs in the southwest Pamirs. (**a**), (**b**), (**c**), (**d**), (**e**), and (**f**) correspond to area, length, *MEF* (minimum elevation at the front), *MaxE* (maximum elevation), slope, and *MAAT* (mean annual air temperature), respectively. Slope, area, and elevation (*MEF* and *MaxE*) were calculated using the RG inventory polygons and AW3D30 DEM in QGIS. Mean annual air temperature (*MAAT*) was computed using the RG inventory polygons and *MAAT* data in QGIS. Asterisks denote statistically significant differences. $n = 242$.

5. Discussion

5.1. Comparison with the Permafrost Zonation Index

We employed the Global Permafrost Zonation Index (*PZI*), based on a global model with a spatial resolution of approximately 1 km [43], to provide a consistent evaluation framework for mapped RGs. Previous studies in the Hindu Kush Himalayan region and the Nepalese Himalaya region have shown a good agreement between the *PZI* and mapped RGs [9,14], with general agreement also reported in the Daxue Shan and the Himachal Himalaya region [20,27]. In this context, we compared the frequency distribution of RGs within the southwestern Pamirs to the *PZI*.

Notably, the *PZI* does not indicate actual permafrost extent [9]. *PZI* values below 0.1 were attributed to the uncertainty margins of the *PZI*—"conservatively estimated areas of potential permafrost extension"—while values of 0.1 or higher indicated permafrost regions [43]. Only two RGs were within the *PZI* uncertainty fringe, indicating that 99% of RGs were located within the permafrost region (Figure 7). Furthermore, as the "habitat suitability" for the genesis and survival of RGs increased, i.e., as the *PZI* approached 1, there was a significant concurrent increase in the frequency of RGs, especially ARGs (Figure 7a). Additionally, Figure 7b demonstrates the spatial distribution of the total area as a function of *PZI* values, suggesting a strong relationship between the habitat suitability for RGs and the total geomorphological area. Regarding the certainty index scores, landforms classified as having high certainty were predominantly concentrated around *PZI* values of 0.6 or higher (ARGs, 74%; TRGs, 72%). Based on this assessment, the identification, mapping, and activity status classification of RGs were in good agreement with the *PZI*.

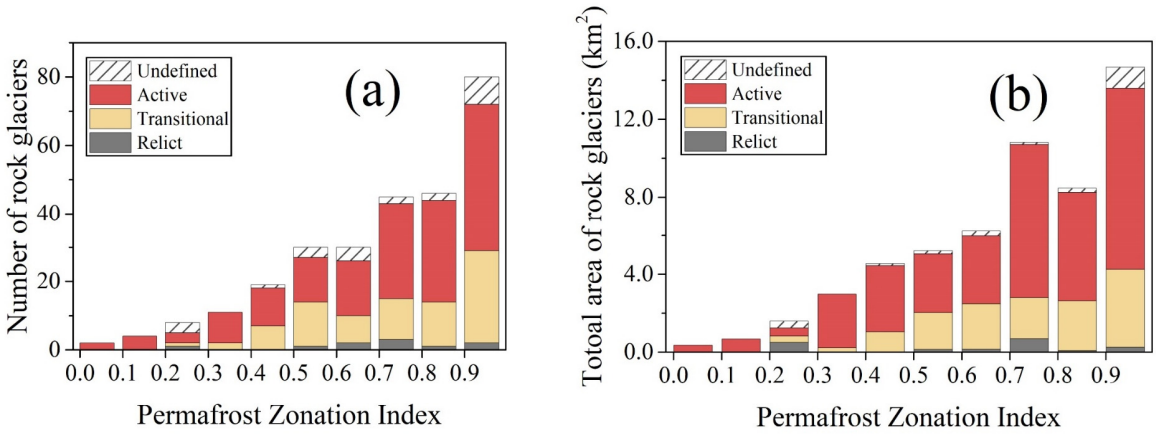

Figure 7. Analysis of the RGs in relation to the Permafrost Zonation Index (*PZI*) for (**a**) the number of landforms and (**b**) the total landform area. See [43] for further information about the *PZI*.

5.2. Environmental Controls on Rock Glaciers

The modeled *MAAT* values of Kohrog and Ishakashim were 7.9 °C and 6.7 °C, respectively, which are 1.4 °C and 0.6 °C lower than the values from other meteorological stations. Conversely, for Dzhaushangoz and Bulun-kul, *MAAT* values were recorded at 0.1 °C and −1.8 °C, 1.5 °C and 3.8 °C higher than the measured values, with the largest discrepancy noted at Bulun-kul, potentially due to the local temperature-lowering effect of nearby lakes (Figure 1c). The uneven temperature distribution across the southwestern Pamirs makes model predictions challenging, yielding more conservative estimates than actual measurements; however, these models successfully capture the overall temperature distribution trends.

Significant negative correlations between RG latitude and *MaxE*, length, and area (Table 3) are dictated by local topographical characteristics. As latitude decreases from north to south, the number of high-altitude RGs increases. This decrease in latitude correlates with an increase in the elevation of mountain ranges and the length of RGs, suggesting that the Shakhdara range offers a more conducive environment for the formation

of RGs and other periglacial landforms compared to the Shughnon range, especially in the western Shakhdara.

Table 3. Correlation matrix of rock glacier variables in the southwestern Pamirs.

	Longitude	**Latitude**	**Area**	**Length**	***MaxE***	**Slope**	***MAAT***
Longitude	1.000						
Latitude	**0.456** **	1.000					
Area	−0.090	**−0.131** *	1.000				
Length	−0.065	**−0.239** **	**0.761** **	1.000			
MaxE	**0.204** **	**−0.248** **	**0.218** **	**0.303** **	1.000		
Slope	0.007	**−0.182** **	**−0.134** *	0.00371	−0.063	1.000	
MAAT	**−0.231** **	−0.050	−0.027	−0.036	**−0.877** **	**0.235** **	1.000

MaxE: maximum elevation; *MAAT*: mean annual air temperature. Note: correlations in bold are significant. * indicates a p-value ≤ 0.05. ** indicates a p-value ≤ 0.01.

The negative correlation between RG length and area with average slope is likely due to the predominance of T-RGs, which typically develop in steep terrains. The negative correlation between *MAAT* and longitude reflects the topographical control, exhibiting a west–high, east–low orientation with the MAAT of RGs in both the Shughnon and Shakhdara ranges exhibiting a decreasing trend from west to east (Figure 1c). Additionally, *MaxE* positively correlates with longitude and negatively with latitude, indicating lower elevations for "habitat suitability" for the genesis of RGs in the northwest direction. This also applies to where RG density is higher (Figure 1c), possibly related to higher precipitation in the northwest, as westerlies are the primary source of precipitation in the area. The western part of the Shakhdara range prevents moisture from the westerlies from entering the northern catchment area of the Shughnon basin, leaving only a few RGs on the leeward slope (eastward) of the Shughnon range, characterized by lower activity, with TRGs and RRGs being more prevalent than in other regions in the southwestern Pamirs (Figure 1c). Glaciers in this part are smaller and sparser compared to the eastern part of the Shughnon range, with U-shaped valleys and glacial lakes downstream of RGs evidencing glacier retreat, indicating higher ice loss in this region and thus lower RG density and activity. Further east into the hinterland, RGs are absent. In summary, the topography of the southwestern Pamirs significantly influences the formation, development, and spatial distribution of RGs.

Moreover, the genesis and evolution of RGs in the southwestern Pamirs are profoundly impacted by glacial erosion landforms [59–62]. This region is rich in paleoglacial remnants and glacial erosional features closely associated with the formation and development of T-RGs, which predominantly originate from small cirques. The freeze–thaw process releases debris from headwalls and side slopes, forming a mixture with meltwater that creeps under gravity to gradually develop into RGs.

5.3. Rock Glacier Kinematics

While many regions within the High Mountain Asia (HMA) area have undergone inventorying studies of RGs, inventories incorporating kinematics remain scarce (Table 4). Among these, RGs in the Daxue Shan, the Tien Shan (Zhetysu, Kazakhstan), and the Central Himalayas have exhibited relatively low activity levels [25,33,34]. Conversely, RGs in the northern Tien Shan (Ile Alatau and Kungöy Ala-Too ranges) are notably active, with 45 out of 550 exhibiting velocities exceeding 100 cm/yr [24]. Similar velocity patterns are observed in the northern Tien Shan of China [23], the western Nyainqêntanglha Range [28], and the western Kunlun Mountains [29], aligning with findings from the southwestern Pamirs. Notably, the western Nyainqêntanglha and western Kunlun Mountains, similar to our study area, are characterized by arid to semi-arid climates, hosting RGs with the same order of velocity magnitudes.

Table 4. Rock glacier kinematics monitoring in the High Mountain Asia region.

Study Area	Observation Period	SAR Dataset	Deformation Rate (cm/yr)	Deformation Direction	Authors
Northern Tien Shan (China)	2007–2009	ALOS PALSAR	maximum: 114; mean: 37	Downslope	[23]
Northern Tien Shan (Ile Alatau and Kungöy Ala-Too)	1998–2018	ERS-1/2, ALOS-1 PALSAR, ALOS-2 PALSAR, and Sentinel-1	maximum: >100	Downslope	[24]
Tien Shan (Zhetysu, Kazakhstan)	2017–2021	Sentinel-1	maximum: 25	Downslope	[25]
Central Himalayas	2018–2019	Sentinel-1	range: 0–7.5	LOS	[33]
Daxue Shan	2015–2019	Sentinel-1	range: 1.0–3.5	Downslope	[34]
Western Nyainqêntanglha Range	2016–2019	Sentinel-1	maximum: 87	Downslope	[28]
Western Kunlun Mountains	2007–2008	ALOS-1 PALSAR	maximum: 127; mean: 17	Downslope	[29]

Investigating the upslope connection units of RGs, glacier-related types (G-RGs and GF-RGs) typically demonstrate higher velocities than talus-related ones (T-RGs and DMS-RGs) (Figure 5a), a finding similar to that in Hu et al. [29] for the western Kunlun Mountains. This velocity discrepancy is likely due to acceleration caused by glacial meltwater during spring and summer [45,52], suggesting a correlation between RG movement and precipitation or meltwater [51,54,55,57,58], supported by their spatial distribution (Figure 1c).

Spatial analysis revealed that RGs in the Shakhdara range are more active than those in the Shughnon range, with the southern slopes of Shakhdara exhibiting greater activity than its northern slopes, a trend reversed in the Shughnon range (Figure 5b). This activity pattern mirrors glacier distribution, with similar observations reported by Reinosch et al. [28] in the western Nyainqêntanglha Range. This distribution may be attributed to the orographic effect, where windward slopes (southern Shakhdara and northern Shughnon) capture most of the moisture, leading to larger glaciers [35] and, consequently, higher RG activity due to increased moisture availability.

RGs respond to mountain-specific variables such as temperature and topography, impacting their velocity. Yet, despite significant environmental variability across the southwestern Pamirs, no substantial differences were found between ARGs and TRGs regarding environmental controls (*MaxE*, *MAAT*, and slope) (Figure 6). Brencher et al. [49] also reported no clear correlation between RG velocities and local *MAAT* or *MAP* in the Uinta Mountains. The kinematics of RGs are influenced by an interplay of factors, including debris supply, snow and meltwater transport rates, thickness, ice content, and shear zone geometry, complicating predictions of RG movements [2,51,57,58,63]. This complex interrelation underscores the challenges in forecasting RG movement.

Although InSAR provides observations of 3D surface deformation components projected along the LOS, it is insensitive to displacement perpendicular to the LOS direction [45,47–49,51]. The LOS for Sentinel-1A's ascending and descending images is approximately 82° and 278° (positive counterclockwise from the north), respectively (Figure 1b). Consequently, displacements toward the north or south are more susceptible to geometric distortions, potentially resulting in underestimated displacement magnitudes [49,51]. In the southwestern Pamirs, 59 RGs are oriented either southward or northward, including 28 ARGs and 18 TRGs. Four RGs displaying no displacement in the interferograms, upon further analysis of optical imagery surface textures, were classified as 'relict'. The remaining nine were categorized as undefined due to the lack of movement features under poor interferogram coherence. Consequently, the primary underestimation risk involves TRGs potentially having actual velocities greater than 10 cm/yr. In summary, the LOS of InSAR restricts the detectable range of RGs, suggesting that the actual displacement of

north–south oriented RGs may be higher. However, this limitation has minimal impact on our study area (18 out of 275).

6. Conclusions

Our inventory presents the inaugural comprehensive documentation of RG characteristics in the southwestern Pamirs. By integrating optical imagery from Google Earth, InSAR from Copernicus Sentinel-1 satellites, and topographic data, a total of 275 RGs were cataloged, covering an area of 55.52 km^2. These RGs predominantly orient northeast and are situated at elevations ranging from 3620 to 5210 m a.s.l., with the majority (80%) located between 4100 and 4800 m, corresponding to a mean *MAAT* value of −6.5 °C. The inventory revealed 213 talus-connected, 26 debris-mantled slope-connected, 14 glacier-connected, and 22 glacier forefield-connected RGs.

The distribution of RGs reflects the interplay between mountain geometry and precipitation patterns, exhibiting a denser distribution in the west and sparser toward the east, with the maximum elevation of the RGs being higher in the southeast and lower in the northwest. The Shakhdara range to the south showcases a greater density of RGs compared to the Shughnon range to the north, especially in the western Shakhdara, where the environment is conducive to the formation of RGs and other periglacial landforms. This is speculated to be due to the Shakhdara range intercepting precipitation from the westerlies.

InSAR analysis identified valid kinematics for 252 RGs, with LOS velocities between 30 and 100 cm/yr being the most common (38%), followed by those in the range of 10–30 cm/yr (23%), and six RGs exceeding LOS velocities of 100 cm/yr. Based on the kinematics, we identified 159 ARGs, 83 TRGs, and 10 RRGs. A comparison between ARGs and TRGs revealed no significant environmental differences (*MaxE*, *MAAT*, and slope), yet the kinematics displayed spatial heterogeneity and variation across upslope connection categories. RGs in the Shakhdara range were more active than those in the Shughnon range, likely due to the Shakhdara range's higher precipitation levels. Glacier-related RGs (G-RGs and GF-RGs) generally exhibited higher LOS velocities than talus-related RGs (T-RGs and DMS-RGs), attributed to the acceleration induced by glacial meltwater during the spring and summer seasons.

Supplementary Materials: The following supporting information can be downloaded at MA, Qiqi (2024), "Rock glacier inventory of the southwestern Pamirs, supported by InSAR kinematics", Mendeley Data, V1, https://data.mendeley.com/datasets/mkvn4nw85g/1.

Author Contributions: Conceptualization, Q.M. and T.O.; methodology, Q.M.; software, Q.M.; validation, Q.M.; formal analysis, Q.M.; data curation, Q.M.; writing—original draft preparation, Q.M.; writing—review and editing, T.O.; visualization, Q.M.; supervision, T.O. All authors have read and agreed to the published version of the manuscript.

Funding: This research received no external funding.

Data Availability Statement: The data that support the findings of this study are openly available. Sentinel-1 Single-Look Complex images used in this study can be downloaded from the Alaska Satellite Facility at https://asf.alaska.edu (accessed on 8 August 2023). The 30 m resolution ALOS World 3D DEM (AW3D30) is available at https://www.eorc.jaxa.jp/ALOS/en/dataset/aw3d30/aw3d30e.htm (accessed on 27 August 2022). High-resolution optical images with 3D representation used in this study are available in the program Google Earth.

Acknowledgments: We are grateful to the providers of free data for this study: the European Space Agency (ESA)/European Commission (EC) Copernicus, the Alaska Satellite Facility (ASF), the Japan Aerospace Exploration Agency (JAXA).

Conflicts of Interest: The authors declare no conflicts of interest.

Appendix A

Table A1. List of interferograms generated from Sentinel-1 data.

Number	Direction	Path	Frame	Master Acquisition Date	Slave Acquisition Date	Time Span (Days)
1	descending	5	466	17 July 2018	29 July 2018	12
2	descending	5	466	24 July 2019	5 August 2019	12
3	descending	5	466	10 September 2019	22 September 2019	12
4	descending	5	466	16 September 2020	28 September 2020	12
5	descending	5	466	29 July 2018	22 August 2018	24
6	descending	5	466	10 August 2018	3 September 2018	24
7	descending	5	466	29 August 2019	22 September 2019	24
8	descending	5	466	23 August 2020	16 September 2020	24
9	descending	5	466	29 July 2018	3 September 2018	36
10	descending	5	466	5 August 2019	10 September 2019	36
11	descending	5	466	23 August 2020	28 September 2020	36
12	descending	5	466	10 August 2018	27 September 2018	48
13	descending	5	466	24 July 2019	10 September 2019	48
14	descending	5	466	17 August 2019	4 October 2019	48
15	descending	5	466	11 August 2020	28 September 2020	48
16	descending	5	466	27 September 2018	29 August 2019	336
17	descending	5	466	29 July 2018	5 August 2019	372
18	descending	5	466	10 September 2019	11 August 2020	336
19	descending	5	466	5 August 2019	11 August 2020	372
20	descending	5	471	17 July 2018	29 July 2018	12
21	descending	5	471	10 September 2019	22 September 2019	12
22	descending	5	471	16 September 2020	28 September 2020	12
23	descending	5	471	10 August 2018	3 September 2018	24
24	descending	5	471	29 August 2019	22 September 2019	24
25	descending	5	471	23 August 2020	16 September 2020	24
26	descending	5	471	29 July 2018	3 September 2018	36
27	descending	5	471	5 August 2019	10 September 2019	36
28	descending	5	471	23 August 2020	28 September 2020	36
29	descending	5	471	10 August 2018	29 August 2019	384
30	descending	5	471	3 September 2018	22 September 2019	384
31	descending	5	471	10 August 2018	22 September 2019	408
32	descending	5	471	22 September 2019	28 September 2020	372
33	descending	5	471	29 August 2019	28 September 2020	396
34	ascending	100	119	23 July 2018	4 August 2018	12
35	ascending	100	119	18 July 2019	30 July 2019	12
36	ascending	100	119	11 August 2019	23 August 2019	12
37	ascending	100	119	29 August 2020	10 September 2020	12
38	ascending	100	119	10 September 2020	22 September 2020	12
39	ascending	100	119	4 August 2018	28 August 2018	24
40	ascending	100	119	11 August 2019	4 September 2019	24
41	ascending	100	119	29 August 2020	22 September 2020	24
42	ascending	100	119	23 July 2018	28 August 2018	36
43	ascending	100	119	4 August 2018	9 September 2018	36
44	ascending	100	119	17 August 2020	22 September 2020	36
45	ascending	100	119	30 July 2019	16 September 2019	48
46	ascending	100	119	17 August 2020	4 October 2020	48
47	ascending	100	119	9 September 2018	30 July 2019	324
48	ascending	100	119	9 September 2018	16 September 2019	372
49	ascending	100	119	23 August 2019	10 September 2020	384
50	ascending	173	118	28 July 2018	9 August 2018	12
51	ascending	173	118	21 August 2018	2 September 2018	12
52	ascending	173	118	16 August 2019	28 August 2019	12

Table A1. *Cont.*

Number	Direction	Path	Frame	Master Acquisition Date	Slave Acquisition Date	Time Span (Days)
53	ascending	173	118	15 September 2020	27 September 2020	12
54	ascending	173	118	16 July 2018	9 August 2018	24
55	ascending	173	118	11 July 2019	4 August 2019	24
56	ascending	173	118	4 August 2019	28 August 2019	24
57	ascending	173	118	22 August 2020	15 September 2020	24
58	ascending	173	118	16 July 2018	21 August 2018	36
59	ascending	173	118	21 August 2018	26 September 2018	36
60	ascending	173	118	10 August 2020	15 September 2020	36
61	ascending	173	118	9 August 2018	26 September 2018	48
62	ascending	173	118	23 July 2019	9 September 2019	48
63	ascending	173	118	16 July 2018	16 August 2019	396
64	ascending	173	118	16 July 2018	28 August 2019	408
65	ascending	173	118	28 August 2019	22 August 2020	360
66	ascending	173	118	16 August 2019	22 August 2020	372

References

1. Berthling, I. Beyond Confusion: Rock Glaciers as Cryo-Conditioned Landforms. *Geomorphology* **2011**, *131*, 98–106. [CrossRef]
2. Haeberli, W.; Hallet, B.; Arenson, L.; Elconin, R.; Humlum, O.; Kääb, A.; Kaufmann, V.; Ladanyi, B.; Matsuoka, N.; Springman, S.; et al. Permafrost Creep and Rock Glacier Dynamics. *Permafr. Periglac. Process.* **2006**, *17*, 189–214. [CrossRef]
3. Humlum, O. Rock Glacier Appearance Level and Rock Glacier Initiation Line Altitude: A Methodological Approach to the Study of Rock Glaciers. *Arct. Alp. Res.* **1988**, *20*, 160–178. [CrossRef]
4. Barsch, D. Permafrost Creep and Rockglaciers. *Permafr. Periglac. Process.* **1992**, *3*, 175–188. [CrossRef]
5. Hassan, J.; Chen, X.; Muhammad, S.; Bazai, N.A. Rock Glacier Inventory, Permafrost Probability Distribution Modeling and Associated Hazards in the Hunza River Basin, Western Karakoram, Pakistan. *Sci. Total Environ.* **2021**, *782*, 146833. [CrossRef]
6. Komatsu, T.; Watanabe, T. Glacier-Related Hazards and Their Assessment in the Tajik Pamir: A Short Review. *Geogr. Stud.* **2014**, *88*, 117–131. [CrossRef]
7. Schoeneich, P.; Bodin, X.; Echelard, T.; Kaufmann, V.; Kellerer-Pirklbauer, A.; Krysiecki, J.-M.; Lieb, G.K. Velocity Changes of Rock Glaciers and Induced Hazards. In Proceedings of the Engineering Geology for Society and Territory—Volume 1; Lollino, G., Manconi, A., Clague, J., Shan, W., Chiarle, M., Eds.; Springer International Publishing: Cham, Switzerland, 2015; pp. 223–227.
8. Baral, P.; Haq, M.A.; Yaragal, S. Assessment of Rock Glaciers and Permafrost Distribution in Uttarakhand, India. *Permafr. Periglac. Process.* **2020**, *31*, 31–56. [CrossRef]
9. Schmid, M.-O.; Baral, P.; Gruber, S.; Shahi, S.; Shrestha, T.; Stumm, D.; Wester, P. Assessment of Permafrost Distribution Maps in the Hindu Kush Himalayan Region Using Rock Glaciers Mapped in Google Earth. *Cryosphere* **2015**, *9*, 2089–2099. [CrossRef]
10. Boeckli, L.; Brenning, A.; Gruber, S.; Noetzli, J. Permafrost Distribution in the European Alps: Calculation and Evaluation of an Index Map and Summary Statistics. *Cryosphere* **2012**, *6*, 807–820. [CrossRef]
11. Buckel, J.; Reinosch, E.; Hördt, A.; Zhang, F.; Riedel, B.; Gerke, M.; Schwalb, A.; Mäusbacher, R. Insights into a Remote Cryosphere: A Multi-Method Approach to Assess Permafrost Occurrence at the Qugaqie Basin, Western Nyainqêntanglha Range, Tibetan Plateau. *Cryosphere* **2021**, *15*, 149–168. [CrossRef]
12. Haq, M.A.; Baral, P. Study of Permafrost Distribution in Sikkim Himalayas Using Sentinel-2 Satellite Images and Logistic Regression Modelling. *Geomorphology* **2019**, *333*, 123–136. [CrossRef]
13. Jones, D.B.; Harrison, S.; Anderson, K.; Whalley, W.B. Rock Glaciers and Mountain Hydrology: A Review. *Earth Sci. Rev.* **2019**, *193*, 66–90. [CrossRef]
14. Jones, D.B.; Harrison, S.; Anderson, K.; Betts, R.A. Mountain Rock Glaciers Contain Globally Significant Water Stores. *Sci. Rep.* **2018**, *8*, 2834. [CrossRef] [PubMed]
15. Jones, D.B.; Harrison, S.; Anderson, K.; Shannon, S.; Betts, R.A. Rock Glaciers Represent Hidden Water Stores in the Himalaya. *Sci. Total Environ.* **2021**, *793*, 145368. [CrossRef] [PubMed]
16. Li, M.; Yang, Y.; Peng, Z.; Liu, G. Assessment of Rock Glaciers and Their Water Storage in Guokalariju, Tibetan Plateau. *Cryosphere* **2024**, *18*, 1–16. [CrossRef]
17. Millar, C.I.; Westfall, R.D.; Delany, D.L. Thermal and Hydrologic Attributes of Rock Glaciers and Periglacial Talus Landforms: Sierra Nevada, California, USA. *Quat. Int.* **2013**, *310*, 169–180. [CrossRef]
18. Immerzeel, W.W.; Lutz, A.F.; Andrade, M.; Bahl, A.; Biemans, H.; Bolch, T.; Hyde, S.; Brumby, S.; Davies, B.J.; Elmore, A.C.; et al. Importance and Vulnerability of the World's Water Towers. *Nature* **2020**, *577*, 364–369. [CrossRef] [PubMed]
19. Pritchard, H.D. Asia's Shrinking Glaciers Protect Large Populations from Drought Stress. *Nature* **2019**, *569*, 649–654. [CrossRef] [PubMed]

20. Pandey, P. Inventory of Rock Glaciers in Himachal Himalaya, India Using High-Resolution Google Earth Imagery. *Geomorphology* **2019**, *340*, 103–115. [CrossRef]
21. Jones, D.B.; Harrison, S.; Anderson, K.; Selley, H.L.; Wood, J.L.; Betts, R.A. The Distribution and Hydrological Significance of Rock Glaciers in the Nepalese Himalaya. *Glob. Planet. Chang.* **2018**, *160*, 123–142. [CrossRef]
22. Bolch, T.; Yao, T.; Bhattacharya, A.; Hu, Y.; King, O.; Liu, L.; Pronk, J.B.; Rastner, P.; Zhang, G. Earth Observation to Investigate Occurrence, Characteristics and Changes of Glaciers, Glacial Lakes and Rock Glaciers in the Poiqu River Basin (Central Himalaya). *Remote Sens.* **2022**, *14*, 1927. [CrossRef]
23. Wang, X.; Liu, L.; Zhao, L.; Wu, T.; Li, Z.; Liu, G. Mapping and Inventorying Active Rock Glaciers in the Northern Tien Shan of China Using Satellite SAR Interferometry. *Cryosphere* **2017**, *11*, 997–1014. [CrossRef]
24. Kääb, A.; Strozzi, T.; Bolch, T.; Caduff, R.; Trefall, H.; Stoffel, M.; Kokarev, A. Inventory and Changes of Rock Glacier Creep Speeds in Ile Alatau and Kungöy Ala-Too, Northern Tien Shan, since the 1950s. *Cryosphere* **2021**, *15*, 927–949. [CrossRef]
25. Kaldybayev, A.; Sydyk, N.; Yelisseyeva, A.; Merekeyev, A.; Nurakynov, S.; Zulpykharov, K.; Issanova, G.; Chen, Y. The First Inventory of Rock Glaciers in the Zhetysu Alatau: The Aksu and Lepsy River Basins. *Remote Sens.* **2023**, *15*, 197. [CrossRef]
26. Zhang, Q.; Jia, N.; Xu, H.; Yi, C.; Wang, N.; Zhang, L. Rock Glaciers in the Gangdise Mountains, Southern Tibetan Plateau: Morphology and Controlling Factors. *Catena* **2022**, *218*, 106561. [CrossRef]
27. Ran, Z.; Liu, G. Rock Glaciers in Daxue Shan, South-Eastern Tibetan Plateau: An Inventory, Their Distribution, and Their Environmental Controls. *Cryosphere* **2018**, *12*, 2327–2340. [CrossRef]
28. Reinosch, E.; Gerke, M.; Riedel, B.; Schwalb, A.; Ye, Q.; Buckel, J. Rock Glacier Inventory of the Western Nyainqêntanglha Range, Tibetan Plateau, Supported by InSAR Time Series and Automated Classification. *Permafr. Periglac. Process.* **2021**, *32*, 657–672. [CrossRef]
29. Hu, Y.; Liu, L.; Huang, L.; Zhao, L.; Wu, T.; Wang, X.; Cai, J. Mapping and Characterizing Rock Glaciers in the Arid Western Kunlun Mountains Supported by InSAR and Deep Learning. *J. Geophys. Res. Earth Surf.* **2023**, *128*, e2023JF007206. [CrossRef]
30. Brardinoni, F.; Scotti, R.; Sailer, R.; Mair, V. Evaluating Sources of Uncertainty and Variability in Rock Glacier Inventories. *Earth Surf. Process. Landf.* **2019**, *44*, 2450–2466. [CrossRef]
31. Buckel, J.; Reinosch, E.; Voigtländer, A.; Dietze, M.; Bücker, M.; Krebs, N.; Schroeckh, R.; Mäusbacher, R.; Hördt, A. Rock Glacier Characteristics Under Semiarid Climate Conditions in the Western Nyainqêntanglha Range, Tibetan Plateau. *J. Geophys. Res. Earth Surf.* **2022**, *127*, e2021JF006256. [CrossRef]
32. Bertone, A.; Barboux, C.; Bodin, X.; Bolch, T.; Brardinoni, F.; Caduff, R.; Christiansen, H.H.; Darrow, M.M.; Delaloye, R.; Etzelmüller, B.; et al. Incorporating InSAR Kinematics into Rock Glacier Inventories: Insights from 11 Regions Worldwide. *Cryosphere* **2022**, *16*, 2769–2792. [CrossRef]
33. Zhang, X.; Feng, M.; Zhang, H.; Wang, C.; Tang, Y.; Xu, J.; Yan, D.; Wang, C. Detecting Rock Glacier Displacement in the Central Himalayas Using Multi-Temporal InSAR. *Remote Sens.* **2021**, *13*, 4738. [CrossRef]
34. Cai, J.; Wang, X.; Liu, G.; Yu, B. A Comparative Study of Active Rock Glaciers Mapped from Geomorphic- and Kinematic-Based Approaches in Daxue Shan, Southeast Tibetan Plateau. *Remote Sens.* **2021**, *13*, 4931. [CrossRef]
35. Mölg, N.; Bolch, T.; Rastner, P.; Strozzi, T.; Paul, F. A Consistent Glacier Inventory for Karakoram and Pamir Derived from Landsat Data: Distribution of Debris Cover and Mapping Challenges. *Earth Syst. Sci. Data* **2018**, *10*, 1807–1827. [CrossRef]
36. Finaev, A.; Shiyin, L.; Weijia, B.; Li, J. Climate Change and Water Potential of the Pamir Mountains. *Geogr. Environ. Sustain.* **2016**, *9*, 88–105. [CrossRef] [PubMed]
37. Maussion, F.; Scherer, D.; Mölg, T.; Collier, E.; Curio, J.; Finkelnburg, R. Precipitation Seasonality and Variability over the Tibetan Plateau as Resolved by the High Asia Reanalysis. *J. Clim.* **2014**, *27*, 1910–1927. [CrossRef]
38. RGIK towards Standard Guidelines for Inventorying Rock Glaciers: Practical Concepts (Version.0). IPA Action Group Rock Glacier Inventories and Kinematics, 10p. Available online: https://bigweb.unifr.ch/Science/Geosciences/Geomorphology/Pub/Website/IPA/CurrentVersion/Current_Practical_Concepts_Inventorying_Rock_Glaciers.pdf (accessed on 20 October 2023).
39. RGIK Towards Standard Guidelines for Inventorying Rock Glaciers: Baseline Concepts (Version 4.2.2). IPA Action Group Rock Glacier Inventories and Kinematics, 13p. Available online: https://bigweb.unifr.ch/Science/Geosciences/Geomorphology/Pub/Website/IPA/CurrentVersion/Current_Baseline_Concepts_Inventorying_Rock_Glaciers.pdf (accessed on 20 October 2023).
40. RGIK Optional Kinematic Attribute in Standardized Rock Glacier Inventories (Version 3.0.1). IPA Action Group Rock Glacier Inventories and Kinematics, 8p. Available online: https://bigweb.unifr.ch/Science/Geosciences/Geomorphology/Pub/Website/IPA/CurrentVersion/Current_KinematicalAttribute.pdf (accessed on 20 October 2023).
41. Benn, D.; Evans, D.J. *Glaciers and Glaciation*, 2nd ed.; Routledge: Abingdon, UK, 2010.
42. Hedding, D.W. Pronival Ramparts. *Prog. Phys. Geogr. Earth Environ.* **2016**, *40*, 835–855. [CrossRef]
43. Gruber, S. Derivation and Analysis of a High-Resolution Estimate of Global Permafrost Zonation. *Cryosphere* **2012**, *6*, 221–233. [CrossRef]
44. Rosen, P.A.; Hensley, S.; Joughin, I.R.; Li, F.K.; Madsen, S.N.; Rodriguez, E.; Goldstein, R.M. Synthetic Aperture Radar Interferometry. *Proc. IEEE* **2000**, *88*, 333–382. [CrossRef]
45. Strozzi, T.; Caduff, R.; Jones, N.; Barboux, C.; Delaloye, R.; Bodin, X.; Kääb, A.; Mätzler, E.; Schrott, L. Monitoring Rock Glacier Kinematics with Satellite Synthetic Aperture Radar. *Remote Sens.* **2020**, *12*, 559. [CrossRef]
46. Yague-Martinez, N.; Prats-Iraola, P.; Rodriguez Gonzalez, F.; Brcic, R.; Shau, R.; Geudtner, D.; Eineder, M.; Bamler, R. Interferometric Processing of Sentinel-1 TOPS Data. *IEEE Trans. Geosci. Remote Sens.* **2016**, *54*, 2220–2234. [CrossRef]

47. Barboux, C.; Delaloye, R.; Lambiel, C. Inventorying Slope Movements in an Alpine Environment Using DInSAR. *Earth Surf. Process. Landf.* **2014**, *39*, 2087–2099. [CrossRef]
48. Villarroel, C.; Tamburini Beliveau, G.; Forte, A.; Monserrat, O.; Morvillo, M. DInSAR for a Regional Inventory of Active Rock Glaciers in the Dry Andes Mountains of Argentina and Chile with Sentinel-1 Data. *Remote Sens.* **2018**, *10*, 1588. [CrossRef]
49. Brencher, G.; Handwerger, A.L.; Munroe, J.S. InSAR-Based Characterization of Rock Glacier Movement in the Uinta Mountains, Utah, USA. *Cryosphere* **2021**, *15*, 4823–4844. [CrossRef]
50. Strozzi, T.; Farina, P.; Corsini, A.; Ambrosi, C.; Thüring, M.; Zilger, J.; Wiesmann, A.; Wegmüller, U.; Werner, C. Survey and Monitoring of Landslide Displacements by Means of L-Band Satellite SAR Interferometry. *Landslides* **2005**, *2*, 193–201. [CrossRef]
51. Liu, L.; Millar, C.I.; Westfall, R.D.; Zebker, H.A. Surface Motion of Active Rock Glaciers in the Sierra Nevada, California, USA: Inventory and a Case Study Using InSAR. *Cryosphere* **2013**, *7*, 1109–1119. [CrossRef]
52. Sorg, A.; Kääb, A.; Roesch, A.; Bigler, C.; Stoffel, M. Contrasting Responses of Central Asian Rock Glaciers to Global Warming. *Sci. Rep.* **2015**, *5*, 8228. [CrossRef] [PubMed]
53. Wirz, V.; Gruber, S.; Purves, R.S.; Beutel, J.; Gärtner-Roer, I.; Gubler, S.; Vieli, A. Short-Term Velocity Variations at Three Rock Glaciers and Their Relationship with Meteorological. *Earth Surf. Dynam.* **2016**, *4*, 103–123. [CrossRef]
54. Arenson, L.; Hoelzle, M.; Springman, S. Borehole Deformation Measurements and Internal Structure of Some Rock Glaciers in Switzerland. *Permafr. Periglac. Process.* **2002**, *13*, 117–135. [CrossRef]
55. Cicoira, A.; Beutel, J.; Faillettaz, J.; Vieli, A. Water Controls the Seasonal Rhythm of Rock Glacier Flow. *Earth Planet. Sci. Lett.* **2019**, *528*, 115844. [CrossRef]
56. Fey, C.; Krainer, K. Analyses of UAV and GNSS Based Flow Velocity Variations of the Rock Glacier Lazaun (Ötztal Alps, South Tyrol, Italy). *Geomorphology* **2020**, *365*, 107261. [CrossRef]
57. Kenner, R.; Pruessner, L.; Beutel, J.; Limpach, P.; Phillips, M. How Rock Glacier Hydrology, Deformation Velocities and Ground Temperatures Interact: Examples from the Swiss Alps. *Permafr. Periglac. Process.* **2020**, *31*, 3–14. [CrossRef]
58. Krainer, K.; He, X. Flow Velocities of Active Rock Glaciers in the Austrian Alps. *Geogr. Ann. Ser. A Phys. Geogr.* **2006**, *88*, 267–280. [CrossRef]
59. Grin, E.; Ehlers, T.A.; Schaller, M.; Sulaymonova, V.; Ratschbacher, L.; Gloaguen, R. 10Be Surface-Exposure Age Dating of the Last Glacial Maximum in the Northern Pamir (Tajikistan). *Quat. Geochronol.* **2016**, *34*, 47–57. [CrossRef]
60. Stübner, K.; Grin, E.; Hidy, A.J.; Schaller, M.; Gold, R.D.; Ratschbacher, L.; Ehlers, T. Middle and Late Pleistocene Glaciations in the Southwestern Pamir and Their Effects on Topography. *Earth Planet. Sci. Lett.* **2017**, *466*, 181–194. [CrossRef]
61. Zabirov, P.A. *Glaciation of Pamir*; Science Press: Beijing, China, 1960.
62. Stübner, K.; Bookhagen, B.; Merchel, S.; Lachner, J.; Gadoev, M. Unravelling the Pleistocene Glacial History of the Pamir Mountains, Central Asia. *Quat. Sci. Rev.* **2021**, *257*, 106857. [CrossRef]
63. Scapozza, C.; Lambiel, C.; Bozzini, C.; Mari, S.; Conedera, M. Assessing the Rock Glacier Kinematics on Three Different Timescales: A Case Study from the Southern Swiss Alps. *Earth Surf. Process. Landf.* **2014**, *39*, 2056–2069. [CrossRef]